Inorganic Chemistry

Article

pubs.acs.org/IC

Mixed-Valent Dicobalt and Iron–Cobalt Complexes with High-Spin Configurations and Short Metal–Metal Bonds

Christopher M. Zall,[†] Laura J. Clouston,[†] Victor G. Young, Jr.,[†] Keying Ding,[†] Hyun Jung Kim,[†,‡] Danylo Zherebetskyy,[†,‡] Yu-Sheng Chen,[§] Eckhard Bill,*[,∥] Laura Gagliardi,*[,†,‡] and Connie C. Lu*[,†]

[†]Department of Chemistry, University of Minnesota, 207 Pleasant Street SE, Minneapolis, Minnesota 55455-0431, United States

[‡]Supercomputing Institute, and Chemical Theory Center, University of Minnesota, Minneapolis, Minnesota, 55455, United States

[§]Advanced Photon Source, Argonne, Illinois 60439, United States

[∥]Max Planck Institut für Chemische Energiekonversion, Stiftstrasse 34-36, 45470, Mülheim an der Ruhr, Germany

Supporting Information

ABSTRACT: Cobalt–cobalt and iron–cobalt bonds are investigated in coordination complexes with formally mixed-valent $[M_2]^{3+}$ cores. The trigonal dicobalt tris(diphenylformamidinate) compound, $Co_2(DPhF)_3$, which was previously reported by Cotton, Murillo, and co-workers (*Inorg. Chim. Acta* **1996**, *249*, 9), is shown to have an energetically isolated, high-spin sextet ground-state by magnetic susceptibility and electron paramagnetic resonance (EPR) spectroscopy. A new tris(amidinato)amine ligand platform is introduced. By tethering three amidinate donors to an apical amine, this platform offers two distinct metal-binding sites. Using the phenyl-substituted variant (abbreviated as L^{Ph}), the isolation of a dicobalt homobimetallic and an iron–cobalt heterobimetallic are demonstrated. The new $[Co_2]^{3+}$ and $[FeCo]^{3+}$ cores have high-spin sextet and septet ground states, respectively. Their solid-state structures reveal short metal–metal bond distances of 2.29 Å for Co–Co and 2.18 Å for Fe–Co; the latter is the shortest distance for an iron–cobalt bond to date. To assign the positions of iron and cobalt atoms as well as to determine if Fe/Co mixing is occurring, X-ray anomalous scattering experiments were performed, spanning the Fe and Co absorption energies. These studies show only a minor amount of metal-site mixing in this complex, and that $FeCoL^{Ph}$ is more precisely described as $(Fe_{0.94(1)}Co_{0.06(1)})(Co_{0.95(1)}Fe_{0.05(1)})L^{Ph}$. The iron–cobalt heterobimetallic has been further characterized by Mössbauer spectroscopy. Its isomer shift of 0.65 mm/s and quadrupole splitting of 0.64 mm/s are comparable to the related diiron complex, $Fe_2(DPhF)_3$. On the basis of spectroscopic data and theoretical calculations, it is proposed that the formal $[M_2]^{3+}$ cores are fully delocalized.

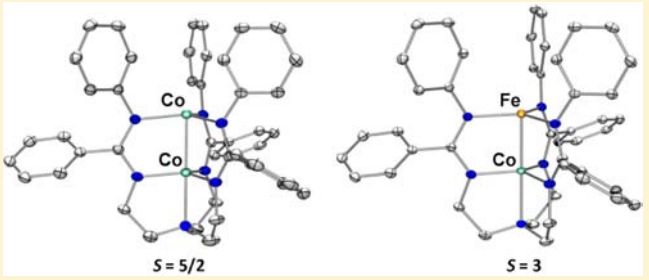

1. INTRODUCTION

Metal–metal bonds are interesting because of their potential roles in heterogeneous and bioinorganic catalysis.[1−3] Given the large number of possible metal pairings and electronic interactions, there is the potential to access a wide range of electronic properties and chemical reactivities. In particular, one sought-after application is the cooperative coupling of metals in multielectron catalysis. Several M-M complexes have demonstrated redox reactions of up to four electrons using second and third-row metals.[4−7] Similar reactivity with first-row metals would be valuable, as they are more earth-abundant and environmentally benign.

Bonds between first-row metals are less well-known than their second- and third-row analogues.[8] By using ligands that stabilize low coordination numbers, that is, 2 to 3, short bonds between first-row metals have been obtained, as demonstrated in the dichromium systems with formal bond orders approaching 5.[9−17] Similar low-coordinate bimetallic complexes of mid-to-late first-row transition metals have in many cases also shown short M-M bonds.[18−23] A classic example is the diiron trigonal lantern complex, $Fe_2(DPhF)_3$ (where DPhF is diphenylformamidinate), reported by Cotton, Murillo, and co-workers.[22] $Fe_2(DPhF)_3$ has an exceptionally short iron–iron bond (2.23 Å) and an unusually high-spin ground state ($S = 7/2$).[24] These were ascribed to the close separation of the metal–metal bonding orbitals engendered by the trigonal ligand field.[25] We recently reexamined this species and confirmed that the octet state is a direct consequence of the π/π^*, δ/δ^*, and σ^* metal–metal d-orbitals being close in energy. Using multiconfigurational wave function calculations, the effective bond order (EBO)[26,27] was determined to be slightly greater than one (EBO = 1.15), which is consistent with the short Fe–Fe bond distance.[28]

We have since expanded our study of first-row metal–metal interactions to cobalt. Dicobalt complexes lacking strongly π-

Received: February 4, 2013
Published: July 31, 2013

   dx.doi.org/10.1021/ic400292g | *Inorg. Chem.* 2013, 52, 9216–9228

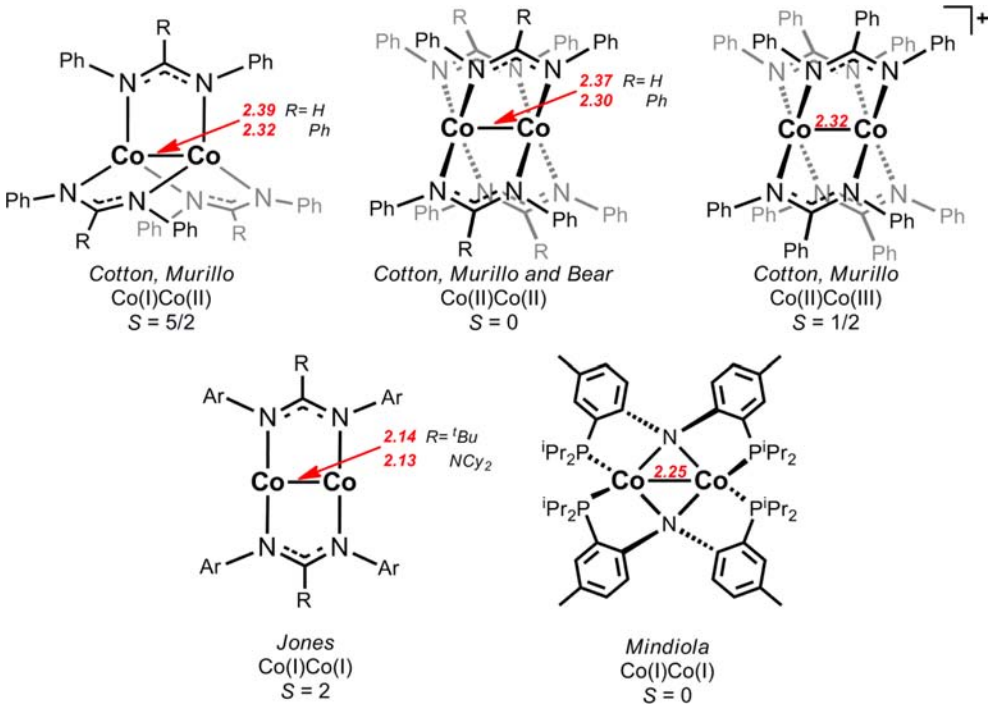

Figure 1. Selected examples of structurally characterized dicobalt complexes with short Co−Co bond lengths (Å, in red). Ground spin states are given.

acidic ligands like CO are uncommon and can exhibit extreme spin states as shown in Figure 1. For instance, two of the complexes with extremely short Co−Co bonds, reported by Jones and Mindiola, are both dicobalt(I,I) systems, but Jones' is high-spin (S = 2) while Mindiola's is low-spin (S = 0).[18,29] Similarly, the tetragonal and trigonal "lantern" complexes $Co_2(DPhF)_4$ and $Co_2(DPhF)_3$, both contain short Co−Co distances, but the former is diamagnetic, while the latter was found to be highly paramagnetic.[19,23,30] Hayton and co-workers have reported a dicobalt(II,II) ketimide complex with a Co−Co bond distance of 2.41 Å that has a temperature-dependent magnetic moment (0.68 to 3.5 μ_B), that would indicate weak antiferromagnetic coupling of the two metal centers.[31] Recently, Thomas and co-workers isolated dicobalt(I,I) and dicobalt(II,I) species with reasonably short bond distances of 2.55 and 2.49 Å, respectively.[32] An intermediate S = 1 state was proposed for the dicobalt(I,I) species, while the dicobalt(II,I) is a low-spin doublet. Additionally, Betley and co-workers have isolated tricobalt clusters, $[Co_3]^{6+}$ and $[Co_3]^{7+}$, with low-spin ground states that arise from strong metal−metal orbital overlap within the trigonal metal core.[33] Related tricobalt complexes in analogous oxidation states but featuring a linear arrangement of metal centers have been shown to undergo thermally induced spin crossover.[34−36] The wide range of spin states and magnetic behavior observed within the relatively small sample of Co−Co bonds illustrates the complexity of bonding between late first-row metal centers.

Even further complexity may be expected when mixed-metal systems are considered. Heterobimetallic complexes are gaining interest as potential organometallic catalysts,[37] and late/late combinations containing bona fide metal−metal bonds are uncommon.[38] Synthetic methods that selectively combine different metal pairs within a fixed ligand environment would further develop magnetostructural relationships, such as the effect of the metal identity on the overall magnetism. For this purpose, we have designed the tris(amidinato)amine ligands ($[L^R]^{3-}$) shown in Figure 2. The multidentate nature of these

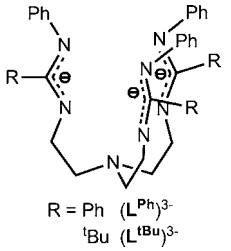

Figure 2. Tris(amidinato)amine ligands ($[L^R]^{3-}$).

ligands controls the coordination number, and the two planes of donor atoms could allow sequential metalations to yield both homo- and heterobimetallic complexes.

Using the phenyl-substituted derivative ($[L^{Ph}]^{3-}$), we have been able to isolate and study the dicobalt species, $Co_2(L^{Ph})$. By comparing $Co_2(DPhF)_3$ (**1**) with $Co_2(L^{Ph})$ (**3**), we show that adding an apical amine donor does not significantly perturb the electronic structure of the dicobalt core. We also report a rare iron−cobalt heterobimetallic, $FeCo(L^{Ph})$ (**4**). The isolation of this complex demonstrates the utility of this ligand architecture for gaining access to heterobimetallics. By comparing **4** to **3**, we show that the swapping of cobalt for iron retains the high-spin, metal−metal bonded configuration of the other trigonal lantern species. Finally, we have used X-ray anomalous scattering experiments to determine the degree of Fe/Co mixing in heterobimetallic **4**. The occupancies of iron and cobalt in the two metal-binding sites have been precisely quantified and are in accord with the structural formula, $(Fe_{0.94}Co_{0.06})$-$(Co_{0.95}Fe_{0.05})L^{Ph}$, where $FeCoL^{Ph}$ represents the majority species.

dx.doi.org/10.1021/ic400292g | Inorg. Chem. 2013, 52, 9216−9228

2. EXPERIMENTAL SECTION

General Considerations. Unless otherwise stated, all manipulations were performed under a dinitrogen atmosphere in a VAC Atmosphere glovebox. Standard solvents were deoxygenated by sparging with dinitrogen and dried by passing through activated alumina columns of a SG Water solvent purification system. *N,N′*-diphenyformamidine (HDPhF) was purchased from Aldrich, dried at 60 °C under vacuum, and recrystallized from diethyl ether. Benzylpotassium[39] and KC_8[40] were prepared according to literature methods. Deuterated solvents were purchased from Cambridge Isotope Laboratories, Inc., degassed via freeze−pump−thaw cycles, dried over activated alumina, and stored over activated 4 Å molecular sieves. All other reagents were purchased from Aldrich or Strem and used without further purification. Elemental analyses were performed by Complete Analysis Laboratories, Inc. (Parsippany, NJ). Inductively Coupled Plasma-Optical Emission Spectrometry (ICP-OES) data were collected at the University of Minnesota Earth Sciences Analytical Geochemistry Lab using a Thermo Scientific iCAP 6500 dual view instrument, with the addition of cesium as a matrix modifier and yttrium as an internal standard. The average of two measurements is reported.

Modified Synthesis of $Co_2(DPhF)_4$. To a solution of HDPhF (11.0 g, 56.1 mmol) in tetrahydrofuran (THF, 100 mL) was added benzylpotassium (7.3 g, 56.1 mmol) in THF (25 mL), forming a light yellow solution immediately. The mixture was stirred for 6 h, and solvent was removed under vacuum. The light yellow solid was rinsed with pentane (3 × 5 mL) and dried under vacuum, giving a light yellow crystalline powder (14.8 g, 85% yield). The ^{1}H NMR spectrum of the solid is consistent with K(THF)[DPhF]: ^{1}H NMR (C_6D_6): δ 8.81 (s, N−C*H*-N, 1H), 7.31 (t, J = 7.6 Hz, *meta*-C*H*, 4H), 6.96 (m, *ortho*- and *para*-CH, 6H), 3.56 (THF, 4H), 1.39 (THF, 4H). To a solution of K(THF)[DPhF] (4.4 g, 14.3 mmol) in THF (80 mL) was added $CoCl_2(THF)_{1.5}$ (1.5 g, 6.3 mmol). The mixture was stirred at room temperature (rt) for 2 h. The precipitate was filtered through Celite (1 cm), and volatiles were removed under vacuum. The brown-green solid was rinsed with diethyl ether (3 × 5 mL), and then dried under vacuum to give a brown powder (1.9 g, 65% yield). ^{1}H NMR (C_6D_6, 500 MHz): δ 8.40 (s, N−C*H*-N, 4H), 6.87 (t, J = 7.0 Hz, *meta*-C*H*, 16H), 6.82 (t, J = 7.0 Hz, *para*-C*H*, 8H), 6.27 (d, J = 7.5 Hz, *ortho*-C*H*, 16H).

*Modified Synthesis of $Co_2(DPhF)_3$ (**1**).* To a solution of $Co_2(DPhF)_4$ (1.4 g, 1.5 mmol) in toluene (50 mL), KC_8 (205 mg, 1.5 mmol) was added, resulting immediately in a black precipitate. After 1 h, the mixture was filtered through a Celite plug, reduced to 10 mL, and cooled at −25 °C to give red-brown crystals (662 mg, 60% yield). ^{1}H NMR (C_6D_6, 500 MHz): δ 175.10 (N−C*H*-N, 3H), 13.00 (*meta*-C*H*, 12H), −26.19 (*para*-C*H*, 6H), −50.16 (*ortho*-C*H*, 12H). UV−vis (toluene): λ_{max}, nm (ε, M^{-1} cm^{-1}): 545 (530), 752 (200), ∼1665 (100). The NIR values are only approximate because of the artifacts created by imperfect subtraction of the solvent background. Anal. Calcd for $C_{39}H_{33}N_6Co_2$: C 66.58; H 4.73; N 11.94. Found C 66.49; H 4.65; N 11.78.

Synthesis of Tris(2-benzamidoethyl)amine. Tris(2-aminoethyl)-amine (tren) (3.2 mL, 21.4 mmol) and NEt_3 (10.3 mL, 73.8 mmol) were combined in a 250 mL RB flask with THF (100 mL) and cooled to 0 °C under ambient atmosphere. Benzoyl chloride (7.8 mL, 67.1 mmol, diluted in 10 mL of THF) was added dropwise, forming a white precipitate. After warming to rt overnight, the precipitate was filtered, then dissolved in $CHCl_3$, washed 4× with distilled water and once with brine, then dried with anhydrous $MgSO_4$. After filtering to collect the supernatant and removing the solvent under vacuum, the resulting pale yellow solid was stirred with diethyl ether and filtered to give a fine white powder (7.7 g, 85% yield). ^{1}H NMR (300 MHz, $CDCl_3$): δ 7.60 (dd, J = 7.2 Hz and 1.2 Hz, 6H), 7.29 (tt, J = 7.5 and 1.2 Hz, 3H), 7.27 (br, 3H), 7.06 (t, J = 8.1 Hz, 6H), 3.55 (quart, J = 5.4 Hz, 6H), 2.72 (t, J = 5.7 Hz, 6H). ESI-TOF-MS (MeOH) m/z: $[M + H]^+$ calc'd for $C_{27}H_{31}O_3N_4$, 459.24; found: 459.28, 481.27 $[M + Na^+]$, 497.27 $[M + K^+]$, 497.27 $[2\ M + H^+]$, 917.58 $[2\ M + Na^+]$ 939.57.

Synthesis of Tris(2-benzimidoylchloroethyl)amine Hydrochloride. Tris(2-benzamidoethyl)amine (7.6 g, 16.6 mmol) was dissolved in CH_2Cl_2 (50 mL) in a 100 mL thick-walled flask. Phosphorus pentachloride (11.8 g, 56.7 mmol) was added, the flask was sealed with a Teflon stopper, and the mixture was refluxed at 50 °C. After 24 h, the volatiles were removed under vacuum. The resulting white residue was washed with toluene (100 mL) and filtered, giving a fine white powder (8.4 g, 85% yield). ^{1}H NMR (300 MHz, $CDCl_3$): δ 12.66 (br, 1H), 7.93 (d, J = 7.5 Hz, 6H), 7.44 (t, J = 7.5 Hz, 3H), 7.27 (t, J = 7.8 Hz, 6H), 4.34 (t, J = 4.8 Hz, 6H), 3.86 (quart, J = 3.9 Hz, 6H).

Synthesis of Tris(2-(N-phenylbenzamidinyl)ethyl)amine (H_3L^{Ph}). Aniline (5.3 g, 57 mmol) was dissolved in CH_2Cl_2 and cooled to −78 °C. A suspension of tris(2-benzimidoylchloroethyl)amine hydrochloride (5.24 g, 9.53 mmol) in CH_2Cl_2 was added dropwise, and the reaction was allowed to slowly warm to rt overnight. The resulting suspension was filtered, giving a fine, white powder, which was washed with CH_3CN (50 mL). After dissolving the powder in water, NaOH (17 mL, 0.1 mol) was added, causing a large amount of white precipitate to form. The precipitate was dissolved in $CHCl_3$, washed three times with water and once with brine, then dried with anhydrous $MgSO_4$. The solvent was removed under vacuum, and the resulting yellow oil was recrystallized from diethyl ether to give a white solid. The solids were dried overnight under vacuum at 60 °C, and finally rewashed with Et_2O to yield a white powder (5.5 g, 80% yield). ^{1}H NMR (500 MHz, CD_3CN): δ 7.22 (t, bridgehead *para*-C-*H*, 3H), 7.12 (m, aryl,12H), 6.99 (t, bridgehead *meta*-C-*H*, 6H), 6.73 (t, apical *para*-C-*H*, 3H), 6.52 (d, apical *ortho*-C-*H*, 6H), 5.53 (br, N-*H*, 3H), 3.56 (br, CH_2, 6H), 2.99 (br, CH_2, 6H). ESI-MS-TOF m/z: $[M + H]^+$ calc'd for $C_{45}H_{46}N_7$, 684.3815; found 684.3806. Anal. Calcd for $C_{45}H_{45}N_7$: C, 79.03; H, 6.63; N, 14.34. Found C 78.92; H 6.53; N 14.26.

Synthesis of Tris(2-pivalamidoethyl)amine. This compound was synthesized in a manner entirely analogous to that of *tris(2-benzamidoethyl)amine*, above, starting from tren (3.1 mL, 20 mmol) and pivaloyl chloride (7.6 mL, 62 mmol). Yield: 6.08 g (76%). ^{1}H NMR (500 MHz, $CDCl_3$): δ 6.175 ppm (br. s, 3H, N*H*), 3.289 ppm (dd, J = 6.25 Hz, J = 12.25 Hz, NH−CH_2, 12H), 2.606 (t, J = 6 Hz, NH−CH_2−CH_2, 12H), 1.194 (s, C(CH_3)$_3$, 27H). ESI-MS-TOF m/z: $[M + H]^+$ calc'd for $C_{21}H_{43}N_4O_3$, 399.3335; found: 399.3491.

Synthesis of Tris(2-pivalimidoylchloroethyl)amine Hydrochloride. This compound was synthesized in a manner entirely analogous to that of *tris(2-benzimidoylchloroethyl)amine*, starting from the tris-amide, above, (5.813 g, 14.6 mmol) and phosphorus pentachloride (9.56 g, 46 mmol). Yield: 6.19 g (86%). ^{1}H NMR (500 MHz, $CDCl_3$): δ 12.978 (s, N-H^+, 1H), 4.025 (t, J = 6 Hz, CH_2−CH_2−N-H^+, 6H), 3.555 (dd, J = 5.5 Hz and 4.5 Hz, CH_2-CH_2−N-H^+, 6H), 1.227 (s, C(CH_3)$_3$, 27H).

Synthesis of Tris(2-(N-phenylpivalamidinyl)ethyl)amine (H_3L^{tBu}). This compound was synthesized in a manner entirely analogous to that of H_3L^{Ph} above, starting from the tris-imidoyl chloride HCl salt, above, (6.19 g, 12.6 mmol) and aniline (4.004 g, 4.3 mmol). Yield: 6.2g (80%). ^{1}H NMR (500 MHz, CD_3CN): δ 7.13 (t, J = 8 Hz, *meta*-C-*H*, 6H), 6.80 (t, J = 7 Hz, *para*-C-*H*, 3H), 6.64 (d, J = 7.5 Hz, *ortho*-C-*H*, 6H), 4.90 (br, N*H*, 3H), 2.59 (br, CH_2, 6H), 2.08 (br, CH_2, 6H), 1.16 (s, C(CH_3)$_3$, 27H). ESI-MS-TOF m/z: $[M + H]^+$ calc'd for $C_{39}H_{58}N_7$, 624.4754; found: 624.4848.

*Synthesis of K(THF)[CoL^{Ph}] (**2**).* H_3L^{Ph} (1.499 g, 2.2 mmol) was dissolved in THF (180 mL) and cooled to −78 °C. Benzylpotassium (895 mg, 6.87 mmol, in 10 mL of THF) was added dropwise over 5 min, during which time the solution turned bright yellow. The solution was stirred for 15 min at −78 °C. $CoCl_2$ (286 mg, 2.2 mmol) was then added. The resulting cloudy green solution was allowed to slowly warm to rt overnight. After 12 h, the mixture was filtered through Celite, and the solvent was removed under vacuum. The solid was washed with toluene (15 mL) and pentane (5 mL), and then dried under vacuum, yielding a bright, lime-green powder (1.60 g, 90% yield). ^{1}H NMR (500 MHz, CD_3CN): δ 70.2 (br, 6H), 59 (br, 6H), 15.2 (s, 6H), 13.3 (br, 6H), 4.36 (s, 6H), 0.41 (s, 3H), −1.86 (s, 3H) −3.76 (s, 6H). UV−vis (THF): λ_{max}, nm (ε, M^{-1} cm^{-1}): 275 (30,900),

dx.doi.org/10.1021/ic400292g | *Inorg. Chem.* 2013, 52, 9216−9228

Table 1. Crystallographic Details for K(THF)[CoL^{Ph}] (2), K[CoL^{tBu}] (2a), Co_2L^{Ph} (3), and FeCoL^{Ph} (4)

	2	2a	3	4
chemical formula	$C_{45}H_{42}CoKN_7(C_4H_8O)$	$C_{39}H_{54}N_7CoK$	$C_{45}H_{42}N_7Co_2$	$C_{45}H_{42}N_7CoFe$
formula weight	850.99	718.92	798.72	795.64
crystal system	monoclinic	orthorhombic	trigonal	trigonal
space group	$P2_1/c$	$Pbca$	$R\bar{3}$	$R\bar{3}$
a (Å)	11.3407(5)	20.568(2)	14.937(1)	14.956(2)
b (Å)	21.550(1)	19.149(2)	14.937(1)	14.956(2)
c (Å)	17.9220(8)	24.290(2)	29.199(2)	29.250(4)
α (deg)	90	90	90	90
β (deg)	92.494(1)	90	90	90
γ (deg)	90	90	120	120
V (Å^3)	4375(9)	9567(2)	5641.8(6)	5666(1)
Z	4	8	6	6
D_{calcd} (g cm^{-3})	1.292	0.998	1.411	1.399
λ (Å), μ (mm^{-1})	0.71073, 0.53	0.71073, 0.475	0.71073, 0.925	0.71073, 0.866
T (K)	173(2)	173(2)	173(2)	173(2)
θ range (deg)	2.29 to 26.47	1.68 to 27.59	1.72 to 28.24	1.72 to 27.50
reflns collected	49826	92104	21580	13888
unique reflns	10090	11058	3083	2900
data/restraint/parameters	10090/92/714	11058/0/439	3083/0/163	2900/0/163
R_1, wR_2 ($I > 2\sigma(I)$)	0.0446, 0.1083	0.0554, 0.1264	0.0378, 0.0952	0.0380, 0.0834

355 (20,350), 598 (80), 618 (80), 780 (12). Anal. Calcd for $C_{45}H_{42}N_7CoK(OC_4H_8)$: C, 69.16; H, 5.92; N, 11.52. Found C, 69.22; H, 6.00; N, 11.61.

Synthesis of K(THF)[CoL^{tBu}] (2a). This compound was synthesized in a manner entirely analogous to that of K(CoL^{Ph}K) (2), above, using H_3L^{tBu} (751 mg, 1.2 mmol), benzylpotassium (475 mg, 3.65 mmol), and $CoCl_2(THF)_{1.5}$ (287 mg, 1.2 mmol). Yield: 812 mg (85%). ^{1}H NMR (500 MHz, CD_3CN): δ 140.9 (br, 6H), 62.8 (br, 6H), 16.0 (br, 27H), 8.02 (s, 6H), 3.11 (s, THF, 1.3H), 2.74 (s, 6H), 1.17 (s, THF, 1.3H) −19.1 (s, 3H). Anal. Calcd for $C_{39}H_{54}N_7CoK(OC_4H_8)$: C, 65.29; H, 7.90; N, 12.39. Found C, 65.21; H, 7.96; N, 12.36.

Synthesis of Co_2L^{Ph} (3). K(THF)[CoL^{Ph}] (325 mg, 0.382 mmol) was dissolved in THF (120 mL) and cooled to −78 °C. Potassium graphite (54 mg, 0.399 mmol) was added as a slurry in THF (3 mL), causing the reaction mixture to turn dark yellow. After stirring for 5 min, $CoBr_2$ (85 mg, 0.39 mmol) was added dropwise as a solution in THF. The mixture was allowed to slowly warm to rt overnight. After 24 h, it was filtered to remove graphite, giving a dark brown filtrate, which was pumped down under vacuum, taken up in toluene, filtered through Celite, and dried to give a brown solid (285 mg, 90% yield). ^{1}H NMR (500 MHz, THF-d_8): δ 158.7 (br, 6H), 104.6 (br, 6H), 24.2 (s, 6H), 16.5 (s, 6H), 10.4 (br s, 6H), −0.09 (s, 3H), −37.1 (s, 3H), −39.05 (br, 6H). ^{1}H NMR (500 MHz, C_6D_6): δ 165.3 (br, 6H), 104.5 (br, 6H), 23.9 (s, 6H), 16.0 (s, 6H), 8.66 (br, 6H), −1.73 (s, 3H), −34.4 (s, 3H), −35.1 (br, 6H). Vis-NIR (THF): λ_{max}, nm (ε, M^{-1} cm^{-1}): 480 sh (2200), 650 sh (430), 850 (150), 1140 (120), 1340 sh (105). Anal. Calcd for $C_{45}H_{42}N_7Co_2$: C, 67.67; H, 5.30; N, 12.28. Found C 67.58; H 5.24; N 12.17.

Synthesis of FeCoL^{Ph} (4). K(THF)[CoL^{Ph}] (260 mg, 0.306 mmol) was dissolved in THF (100 mL) and cooled to −78 °C. Potassium graphite (45.2 mg, 0.334 mmol) was added as a slurry in THF (3 mL), causing the reaction mixture to turn dark yellow. After stirring for 5 min, $FeBr_2$ (72.0 mg, 0.334 mmol) was added dropwise as a solution in THF. The mixture was allowed to slowly warm to rt overnight. After 12 h, it was filtered to remove graphite, giving a dark purple filtrate, which was pumped down under vacuum, taken up in benzene, filtered through Celite, and dried under vacuum to give a purple powder (225 mg, 90% yield). ^{1}H NMR (500 MHz, C_6D_6): δ 172.6 (br, 6H), 127.0 (br, 6H), 23.13 (s, 6H), 11.40 (s, 6H), 6.94 (br s, 6H), 0.78 (s, 3H), 24.1 (s, 3H), −31.5 (br, 6H). Vis-NIR (THF): λ_{max}, nm (ε, M^{-1} cm^{-1}): 514 (3000), 1050 (175). Anal. Calcd for $C_{45}H_{42}N_7CoFe$: C, 67.93; H, 5.32; N, 12.32. Found C 67.86; H 5.28; N 12.23. ICP-OES (wt %): Fe, 5.5157; Co, 8.1954.

X-ray Crystallographic Data Collection and Refinement of the Structures. Single crystals of K(THF)[CoL^{Ph}] (2), K[CoL^{tBu}] (2a), Co_2L^{Ph} (3), and FeCoL^{Ph} (4) were grown by vapor diffusion of Et_2O or pentane into concentrated THF solutions of 2, 2a, 3, and 4 at rt, respectively. Green blocks of 2 (0.60 × 0.30 × 0.20 mm^3) and 2a (0.50 × 0.38 × 0.18 mm^3), a brown block of 3 (0.5 × 0.5 × 0.4 mm^3), and a red plate of 4 (0.36 × 0.20 × 0.06 mm^3) were placed on the tip of a glass capillary and mounted on a Bruker APEX-2 Platform CCD diffractometer for data collection at 173(2) K. The data collection was carried out using Mo−Kα radiation (graphite monochromator). The data intensity was corrected for absorption and decay (SADABS). Final cell constants were obtained from least-squares fits of all measured reflections. The structure was solved using SHELXS-97 and refined using SHELXL-97. A direct-methods solution was calculated which provided most non-hydrogen atoms from the E-map. Full-matrix least-squares/difference Fourier cycles were performed to locate the remaining non-hydrogen atoms. All non-hydrogen atoms were refined with anisotropic displacement parameters, respectively. Hydrogen atoms were placed ideally and refined as riding atoms with relative isotropic displacement parameters. For 2a, the PLATON program, SQUEEZE function, was used to remove disordered solvent comprising two molecules of THF/Et_2O per asymmetric unit.[41] A total of 672 electrons were removed in a total volume of 2976 Å^3 per unit cell, equally distributed between two positions at (0, 0, 0) and (0.3, 0.3, 0.5) in the asymmetric unit. The number of electrons is consistent with removal of 12 ether and 4 THF molecules per unit cell, which is consistent with the 3:1 ratio observed by ^{1}H NMR spectroscopy. Crystallographic data are summarized in Table 1.

Anomalous Diffraction Data Collection and Refinement of Fe/Co Occupancies in 4. A single crystal of 4 was mounted on a glass fiber and cooled to 100 K using an Oxford Instruments Cryojet cryostat. The Bruker D8 diffractometer, integrated with an APEX-II CCD detector, was modified for synchrotron use at the ChemMatCARS 15-ID-B beamline at the Advanced Photon Source (Argonne National Laboratory). Diffraction data were collected at seven different energies with 0.3 s frames while manually attenuating the beam to minimize overages of individual pixels. The scan at 30.0 keV (λ = 0.41328 Å), which is energetically well above the atomic absorption energies, gave a least-squares refinement of all model positional- and displacement parameters to 0.5 Å resolution. To determine the compositions of Fe/Co at the two independent metal sites, a total of six anomalous diffraction data sets were collected near the absorption K-edges of Fe and Co (3 each): one preceding the Fe K-edge at 7.062 keV (1.75567 Å); one at the Fe K-edge 7.112 keV (λ

dx.doi.org/10.1021/ic400292g | Inorg. Chem. 2013, 52, 9216−9228

= 1.74332 Å); one following the Fe K-edge at 7.162 keV (1.73115 Å); one preceding the Co K-edge at 7.659 keV (1.61882 Å); one at the Co K-edge at 7.709 keV (λ = 1.60832 Å); and one following the Co K-edge at 7.759 (1.59795 Å). The anomalous diffraction can readily distinguish Fe/Co compositions at the two metal sites because of the expected differences in the $\Delta f'$ and $\Delta f''$ values for these two elements, as shown in Figure 3. Basically, $\Delta f'$ and $\Delta f''$ values of an element

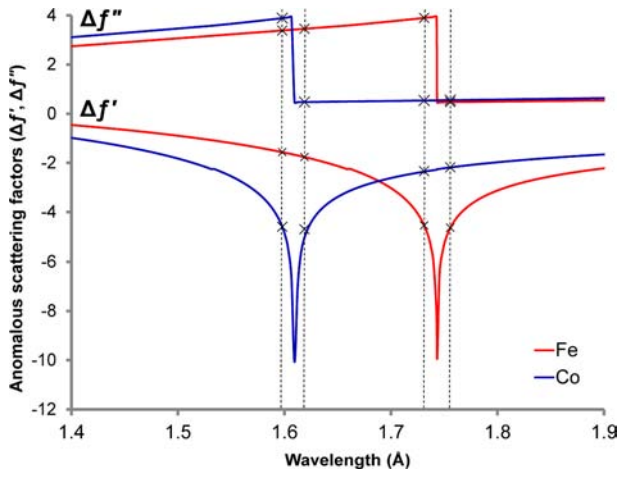

Figure 3. Anomalous dispersion corrections to normal scattering factors, including the real ($\Delta f'$) and imaginary ($\Delta f''$) components, for Fe (red) and Co (blue) as a function of wavelength (Å). The four dotted lines are the experimental wavelengths for the anomalous experiments, which were selected to span the Fe and Co absorption edge energies. The cross marks (×) indicate the Fe and Co anomalous scattering factor values used in the least-squares refinement to determine the metal occupancies.

change dramatically near the element's absorption edge, but, for other element(s), they remain relatively constant. Each of the anomalous diffraction data sets thus provides a different view of the electrons present at both sites. Since metal K-edges may shift slightly within coordination complexes, the data collected at the metal K-edges are less reliable than those collected above and below the K-edge energies. Hence, only four of the six data sets were used in a least-squares refinement to determine the Fe/Co occupancies at the two metal sites. GSAS-II was employed for these least-squares refinements because it allows multiple diffraction data sets as an input with subsequent refinement using a common crystallographic model.[42] The 30 keV data was refined using a structural model of **4** that had been determined at 173 K (see above). The converged positional- and displacement parameters were than frozen, so that only the Fe/Co occupancies of the two independent sites could be refined simultaneously using the six anomalous diffraction data sets. The refinement results shows mixed occupancies of the metal elements at both sites with significantly higher percentages of Fe at the top site (Fe 93.8%, Co 6.2%) and Co at the bottom site (Co 95.2%, Fe 4.8%) (see Supporting Information). Hence, the precise structural formula of **4** is $(Fe_{0.94(1)}Co_{0.06(1)})(Co_{0.95(1)}Fe_{0.05(1)})L^{Ph}$. Crystallographic details are as follows: empirical formula, $C_{45}H_{42}N_7Co_{1.01}Fe_{0.99}$; fw, 795.66; trigonal; $R\bar{3}$; a,b = 14.9092(6) Å, c = 29.191(1) Å; α,β = 90°, γ = 120°; V, 5619.4(5) Å^3; Z, 6; D_{calcd}, 1.411 g/cm^3; μ, 0.205 mm^{-1}; λ, 0.41328 Å; T, 100(2) K; θ, 1.86−20.30°; reflns collected, 45843; unique reflns, 6123; data/restraint/parameters, 6123/0/163; R_1,wR_2 ($I > 2\sigma(I)$): 0.0377, 0.0891.

Physical Measurements. NMR spectra were collected on a Varian Inova 500 MHz spectrophotometer. Visible and near-infrared absorption data were collected on a Cary-14 spectrophotometer. UV-wavelength absorption spectra were collected on a Cary 300 Bio UV−visible spectrophotometer. Perpendicular-mode X-band EPR spectra were recorded on a Bruker EPP 300 spectrometer equipped with an Oxford ESR 910 liquid helium cryostat and an Oxford temperature controller. X-band EPR spectra were simulated using the ESIM program written by Eckhard Bill. Mössbauer data were recorded on an alternating constant acceleration spectrometer. The minimum experimental line width was 0.24 mm s^{-1} (full width at half-height). The ^{57}Co/Rh source (1.8 GBq) was positioned at rt inside the gap of the magnet system at a zero-field position. Isomer shifts are quoted relative to iron metal at 300 K.

Magnetic susceptibility data were measured from powder samples of solid material in the temperature range 2−300 K by using a SQUID susceptometer with a field of 1.0 T (MPMS-7, Quantum Design, calibrated with standard palladium reference sample, error <2%). Multiple-field variable-temperature magnetization measurements were done at 1 T, 4 T, and 7 T also in the range 2 to 300 K with the magnetization equidistantly sampled on a 1/T temperature scale. The experimental data were corrected for underlying diamagnetism by use of tabulated Pascal's constants ($\chi_{dia} < 0$),[43,44] as well as for temperature-independent paramagnetism ($\chi_{TIP} > 0$).[45] The latter was adjusted such that χ^*T was obtained constant above 50 K after subtraction of χ_{TIP}. The susceptibility and magnetization data were simulated with the program julX for exchange coupled systems.[46] The simulations are based on the usual spin-Hamiltonian operator for mononuclear complexes with spin S:

$$\hat{H} = g\beta\hat{\vec{S}}\cdot\vec{B} + D\left[\hat{S}_z^{\,2} - \frac{1}{3}S(S+1) + E/D(\hat{S}_x^{\,2} - \hat{S}_y^{\,2})\right] \quad (1)$$

where g is the average electronic g value, and D and E/D are the axial zero-field splitting and rhombicity parameters. Magnetic moments are calculated after diagonalization of the Hamiltonian from the eigenfunctions using the Hellman-Feynman theorem $\vec{\mu}_i(\vec{B}) = \langle\psi_i|\mathrm{d}H/\mathrm{d}\vec{B}|\psi_i\rangle$. Intermolecular interactions were considered by using a Weiss temperature, Θ_W, as perturbation of the temperature scale, $kT' = k(T - \Theta_W)$ for the calculation. Powder summations were done by using a 16-point Lebedev grid. Because the program is presently not dimensioned for individual spins larger than 5/2, we reproduced the septet ground state of **4** by adopting two individual spins $S_1 = S_2 = 3/2$ with an arbitrarily chosen large, positive exchange coupling constant, J = +200 cm^{-1}, which is defined as:

$$\hat{H} = -2J[\hat{\vec{S}}_1\cdot\hat{\vec{S}}_2] + \hat{H}_{e,1} + \hat{H}_{e,2}. \quad (2)$$

This approach is physically equivalent to a simulation with an isolated total spin S = 3 for the bimetallic, because the resulting septet ground state is energetically well isolated by an energy gap ΔE of 1200 cm^{-1} or more from the other calculated total spin manifolds ($\Delta E/k$ > 1700 K), such that Boltzmann population of other manifolds is negligible up to ambient temperature (300 K).

Computational Methods. *DFT Calculations.* Bimetallic **4** was studied using density functional theory (DFT) and the complete active space self-consistent field (CASSCF) method,[47] followed by a multiconfigurational second-order perturbation theory (CASPT2) method.[48] Previous studies on similar systems have demonstrated that this approach is successful in predicting accurate results for ground and electronically excited states of bimetallic systems.[49−52] Gas-phase geometry optimizations were performed for the various possible spin states at the DFT level of theory with the use of the Perdew−Burke−Ernzerhof (PBE) exchange-correlation functional[53] within the TURBOMOLE 6.1 program package.[54] For C and H atoms, the double-ζ quality basis set def-SV(P) was used, whereas the triple-ζ quality basis set def-TZVP was employed for N and additional polarized functions where introduced by using def-TZVPP for Fe and Co. The DFT calculations were performed with the broken symmetry option (unrestricted calculations) and the resolution-of-the-identity (RI) approximation for several spin states.[55]

CASSCF/CASPT2 Calculations. All CASSCF/CASPT2 calculations were performed with the MOLCAS-7.4 package[56] using the DFT-optimized structure. The relativistic all-electron ANO-RCC basis sets[57,58] were used for all elements. In all of these calculations, the ANO-RCC-VDZP basis set was used for Fe, Co, and N while the ANO-RCC-MB basis set was used for C and H. Scalar relativistic effects were included by using the Douglas−Kroll−Hess Hamil-

dx.doi.org/10.1021/ic400292g | Inorg. Chem. 2013, 52, 9216−9228

Scheme 1

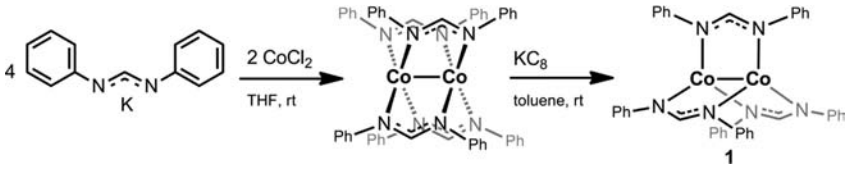

Scheme 2

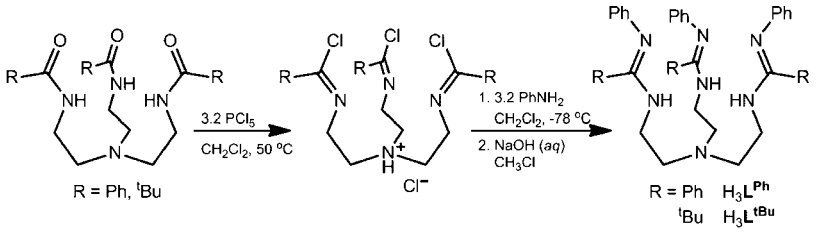

Scheme 3

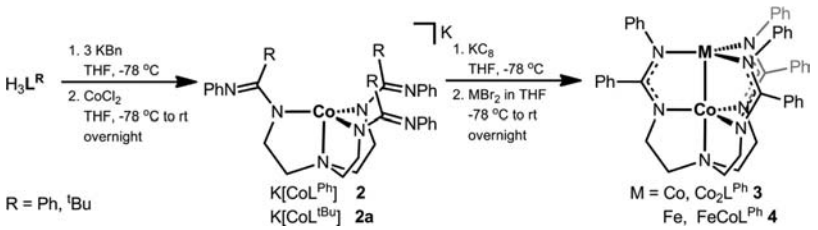

tonian.[59] The two-electron integral evaluation was simplified by employing the Cholesky decomposition technique.[60−62] To avoid intruder states, an imaginary level shift of 0.2 au was used in the CASPT2 calculations.[63] A full valence complete active space consisting 14 d-electrons in 12 orbitals (14,12) was used. The 12 orbitals consisted of the ten 3d orbitals of the two metal centers and two virtual orbitals comprising the 4d Co orbitals.

3. RESULTS

Synthesis. Cotton, Murillo, and co-workers reported the one-pot synthesis of $Co_2(DPhF)_3$ (**1**) from the Co(II) precursor, $CoCl_2(HDPhF)_2$.[23] Presumably, the reaction occurs according to the balanced reaction,

$$2CoCl_2(HDPhF)_2 \xrightarrow[-78\ to\ 0\ °C]{NaBEt_3H} \xrightarrow[-78\ °C\ to\ rt]{4^nBuLi} Co_2(DPhF)_3 + NaCl + 3LiCl + Li(DPhF) + 0.5H_2 + BEt_3$$

wherein $NaBEt_3H$ acts as the reducing agent, nBuLi deprotonates the amidine ligands, and the extra amidinate ligand is lost as Li(DPhF). In our hands, this reaction gave variable yields of **1**, which is not so surprising given the complicated set of elementary reactions that is needed to form the mixed-valent bimetallic. To obtain **1** more reliably, we developed the simplified procedure shown in Scheme 1 that utilizes the known tetragonal Co(II)Co(II) analogue, $Co_2(DPhF)_4$. By reducing $Co_2(DPhF)_4$ with one equivalent of KC_8, **1** can be generated cleanly and isolated in ∼60% crystalline yield. K(DPhF) is presumed to be the byproduct. The loss of an amidinate ligand from $Co_2(DPhF)_4$ has been previously observed in a complementary ligand-abstraction reaction.[19] Specifically, the salt metathesis of $Co_2(DPhF)_4$ with $AgPF_6$ proceeds with loss of 0.5 equiv of $[Ag(DPhF)]_2$ to the trigonal dicobalt salt, $[Co_2(DPhF)_3(CH_3CN)_2]PF_6$, wherein the Co···Co separation of 2.885(1) Å is too long to have any significant Co−Co interaction. Of note, the loss of a ligand upon reduction, as observed here, had not been reported.

We have been interested in developing a general synthetic strategy to access other high-spin bimetallics, and for this purpose, the tris(amidinato)amine ligands were designed. The tris(amidine)amine proligands, H_3L^{Ph} and H_3L^{tBu}, are, to our knowledge, previously unknown. Their syntheses consist of three relatively simple and good-yielding reactions from commercially available tris(2-aminoethyl)amine, or tren. First, benzoyl or pivaloyl chloride (3.4 equiv.) is added to tren in the presence of excess triethylamine to generate the tris(amide)-amine species. Second, the amide groups are transformed into imidoyl chloride functionalities using phosphorus pentachloride (Scheme 2). Third, nucleophilic substitution of aniline at each imidoyl chloride group produces the neutral proligands, H_3L^{Ph} and H_3L^{tBu} after a basic workup.

From the H_3L^{Ph} proligand, the new dicobalt complex, Co_2L^{Ph} (**3**), is readily obtained after two sequential metalation reactions (Scheme 3). In both metalations, the cobalt sources are simple cobalt dihalides. Based on NMR analysis of the crude products, $CoCl_2$ reacts more cleanly than $CoBr_2$ in the first metalation, while $CoBr_2$ is preferred in the second. The first metalation involves deprotonation of the proligand with benzylpotassium followed by a salt metathesis reaction with $CoCl_2$ to yield the monoanionic monocobalt complexes, $K(THF)[CoL^{Ph}]$ (**2**). The second metalation involves in situ reduction of **2** with KC_8, followed by the dropwise addition of a $CoBr_2$ solution in THF. A similar strategy is successful for obtaining the *t*-butyl derivative, $K(THF)[CoL^{tBu}]$ (**2a**), though preparation of the dicobalt counterpart $Co_2(L^{tBu})$ has been unsuccessful. Attempts to make Co_2L^{tBu} gave a product with too many peaks in the proton NMR spectrum, which is inconsistent with the desired, C_3-symmetric Co_2L^{tBu}.

dx.doi.org/10.1021/ic400292g | Inorg. Chem. 2013, 52, 9216−9228

The mononuclear cobalt species, **2**, is a potential platform for the synthesis of other bimetallics. Following a similar synthetic protocol as that for **3**, the heterobimetallic $FeCoL^{Ph}$ **4** can be prepared by using $FeBr_2$ in the second metalation step.

NMR and Vis-NIR Data. The ^{1}H NMR data for the trigonal dicobalt complexes **1** and **3** is consistent with 3-fold or higher symmetry (Figure 4). Compound **1** exhibits four resonances,

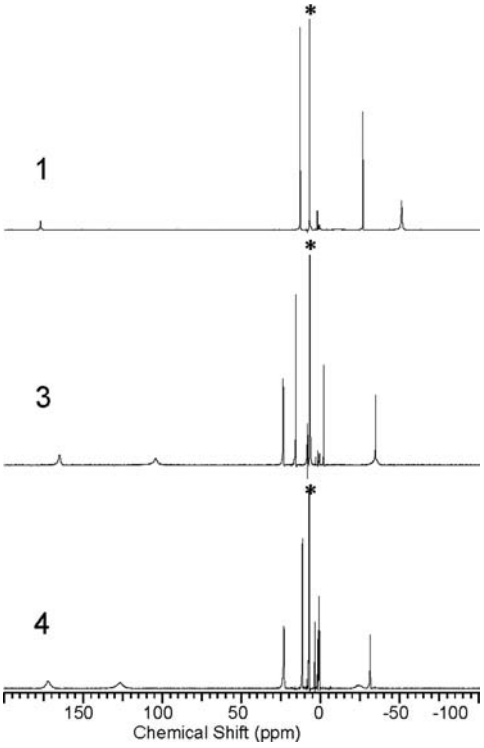

Figure 4. ^{1}H NMR (500 MHz, C_6D_6) spectra of dicobalt complexes **1** (top) and **3** (middle), as well as the iron−cobalt complex **4** (bottom). The residual solvent resonance is indicated by an asterisk.

ranging from −50.2 to 175.1 ppm, where the most downfield peak is assigned to the proton in the DPhF backbone (i.e., NC*H*N) based on its integration. The number of resonances is consistent with the idealized D_{3h} symmetry expected for **1**. For **3**, eight signals are observed, which is consistent with the expected C_3 symmetry in solution. The proton shifts range from −35.1 to 165.3 ppm, but the most distinctive feature is the pair of broad resonances at downfield shifts of 165.3 and 104.5 ppm. Each broad peak integrates to 6 protons. Because these two resonances have no analogues among the peaks observed for **1**, they likely correspond to either the two methylene groups of the tren backbone or the *meta*/*ortho* resonances of the bridgehead phenyl group in the amidinate moiety, that is, NC*Ph*N.

The ^{1}H NMR spectrum for the iron−cobalt species **4** is very similar to that of dicobalt **3** (Figure 4). In comparing the two bimetallics, the most shifted peaks are the two downfield resonances at 172.6 and 127.0 ppm. The fact that these two peaks are highly sensitive to the swapping of the top metal center could suggest that they correspond to the bridgehead phenyl group rather than the tren backbone.

The dicobalt complexes **1** and **3** are red-brown and brown, respectively, while the iron−cobalt compound **4** is purple. As shown in Figure 5, **1** has two relatively weak absorptions in the visible (Vis) region at λ_{max} = 545 and 750 nm (ε = 530, 200

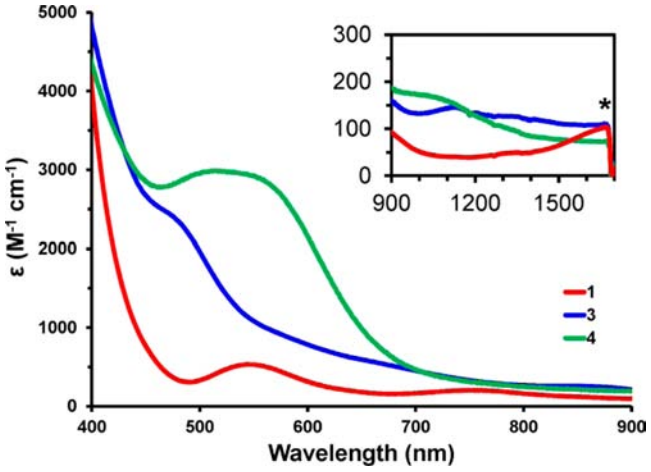

Figure 5. Vis-NIR spectra of dicobalt complexes **1** (in red), **3** (in blue), and iron−cobalt **4** (in green) in toluene at rt. Inset shows the NIR region (ε vs nm). An asterisk marks the onset of imperfect background subtraction. See text for details.

M^{-1} cm^{-1}, respectively), and an even weaker absorption in the near-infrared (NIR) region at $\lambda_{max} \sim$ 1665 nm ($\varepsilon \sim$ 100 M^{-1} cm^{-1}). The electronic absorption spectrum of **1** is similar to $Fe_2(DPhF)_3$, which exhibited four bands between 650 and 1250 nm. Based on symmetry and theoretical analyses, these electronic transitions in $Fe_2(DPhF)_3$ were assigned as spin- and dipole-allowed *d*-*d* excitations in a fully delocalized metal−metal bonding scheme.[28] By analogy, the Vis/NIR bands exhibited by **3** are tentatively assigned as d-d transitions of the dicobalt core.

The electronic absorption of **3** is the least distinctive, resembling a broad curve that tapers gradually into the Vis/NIR region. Four features can be distinguished: two shoulders at 480 and 650 nm, and two weak bands at 850 and 1140 nm (ε = 150, 120 M^{-1} cm^{-1}, respectively). Complex **4** has intense absorptions centered at 514 nm ($\varepsilon \sim$ 3,000 M^{-1} cm^{-1}) and a weak band at 1050 nm (ε = 175 M^{-1} cm^{-1}). For **3** and **4**, the weak NIR bands are likely to be *d*-*d* transitions of a high-spin, delocalized dicobalt and iron−cobalt core, respectively. The visible transitions of **3** and **4** are highly intense and are likely to be charge-transfer bands between the metal and the amidinate ligands. The shifting of the band to higher energies for dicobalt relative to iron−cobalt would be more consistent with metal-to-ligand charge-transfer (MLCT).

X-ray Diffraction and Anomalous Scattering Studies. En route to the M-Co bimetallics, the monocobalt anion, $K(THF)[CoL^{Ph}]$ **2**, was isolated as a bright green solid. Single crystals of **2** were grown by vapor diffusion of pentane into a concentrated THF solution and analyzed by X-ray diffraction. A single crystal of the t-butyl analogue, $K[CoL^{tBu}]$ **2a**, has also been analyzed. The solid-state structures of **2**·THF and **2a** are shown in Figures 6 and 7. In both structures, the ligand is tetradentate in a $\kappa N_{ax}\kappa^3 N_{eq}$-coordination mode. The geometry at the cobalt center is trigonal monopyramidal, which is typical of Co(II) centers supported by related tris(amido)amine ligands.[64−66] The $Co-N_{eq}$ bond distances are slightly longer in **2a** (2.01 to 2.02 Å) than in **2** (1.96 to 1.98 Å). We were gratified to observe that the three remaining nitrogen atoms of the ligand remain unchelated with respect to cobalt. They do bind the potassium countercation, creating a continuous, two-dimensional network in the crystal lattice. Conceivably, these

dx.doi.org/10.1021/ic400292g | *Inorg. Chem.* 2013, 52, 9216−9228

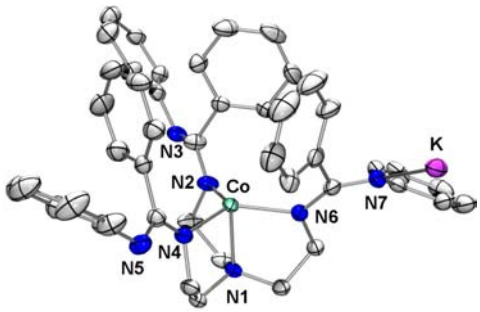

Figure 6. Solid-state structure of **2** at 50% probability. Hydrogen atoms and THF molecule (coordinated to K) are omitted for clarity. Only the shortest K–N bond is shown. Selected bond distances (Å): Co–N1 2.108(2), Co–N2 1.958(2), Co–N4 1.978(2), Co–N6 1.983(2), K–N7 2.845(2); selected bond angles (deg): N2–Co–N4 117.12(9), N4–Co–N6 122.32(9), N2–Co–N6 118.11(9), N1–Co–N2 85.28(8), N1–Co–N4 84.52(7), N1–Co–N6 84.56(8).

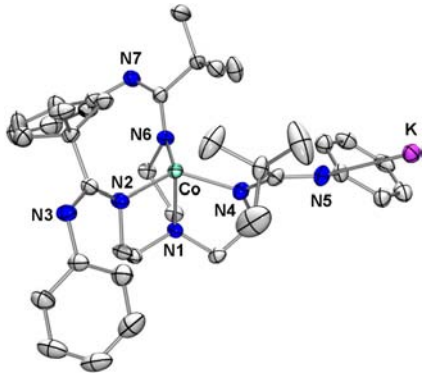

Figure 7. Solid-state structure of **2a** at 50% probability. Hydrogen atoms are omitted for clarity. Only the shortest K–N bond is shown. Selected bond distances (Å): Co–N1 2.094(2), Co–N2 2.013(2), Co–N4 2.018(2), Co–N6 2.022(2), K–N5 2.785(2); selected bond angles (deg): N2–Co–N4 118.89(9), N4–Co–N6 119.15(9), N2–Co–N6 119.99(9), N1–Co–N2 85.70(8), N1–Co–N4 85.11(9), N1–Co–N6 85.14(9).

donors are available to bind a second metal center that can be introduced in a second metalation step.

Cotton, Murillo, and co-workers previously reported the molecular structure of **1**, which crystallized in the triclinic space group $P\bar{1}$.[19] Inspection of the Co–N_{eq} bond lengths and the N_{eq}–Co–N_{eq} angles in **1** reveals a slight distortion from 3-fold symmetry about the Co–Co axis (Table 2). A similar distortion was observed in the diiron analogue $Fe_2(DPhF)_3$ and was attributed to crystal packing forces.[22] In contrast to **1**, our dicobalt **3** complex crystallizes in the trigonal space group $R\bar{3}$, resulting in perfect C_3 symmetry (Figure 8, Table 2).

One notable difference between the experimental structures of **1** and **3** is the significant contraction in the Co–Co bond length (Δ_{Co-Co} = 0.09 Å) of **3**. The shorter Co–Co bond distance in **3** is surprising because one normally expects the addition of an axial ligand to attenuate the metal–metal interaction via the ligand's *trans* influence. For example, it is well-established that adding axial donors to dichromium tetracarboxylates significantly increases the Cr–Cr bond length.[8] In **3**, the presence of the axial donor and the asymmetric nature of the amidinate donors differentiate the two cobalt centers. The Co–N_{eq} bond distances are significantly shorter for the cobalt center that is bound to the axial amine donor. In addition, the cobalt atoms are significantly displaced out of the planes defined by the equatorial nitrogen donors, away from the axial donor.

Akin to **3**, iron–cobalt **4** crystallizes in the same space group, $R\bar{3}$, with C_3 symmetry (Figure 9, Table 2). Disorder that arises from metal-mixing can be challenging, if not impossible, to detect by standard X-ray diffraction methods when the metals have similar atomic numbers as in the case of **4**. To differentiate iron and cobalt, we turned to X-ray anomalous scattering techniques, which have been shown to be effective at quantifying metal-mixing disorder within single crystals.[67,68] In these studies, several sets of X-ray diffraction data were collected on a single crystal of **4**, with the wavelength of the X-ray source tuned to cover a range of energies near the K-edge absorption energies of iron and cobalt. A final data set was collected at significantly higher energy. These studies exploit the fact that anomalous dispersion contributions to the scattering factor change substantially near the scattering atom's absorption edge energy. Since edge energies are significantly different even for similar metals such as iron and cobalt, the occupancies of each metal at a specific crystallographic site can be determined. (Figure 3). We have determined the ratios of Fe/Co in the two metal sites by conducting least-squares refinement of four anomalous diffraction data collected at the different wavelengths simultaneously. This method varies from other literature reports that calculate Fourier difference maps (or apparent f') at each wavelength.[67,69] The current method has the benefit of reporting refined values with standard uncertainties and provides a straightforward scaling of the different anomalous data sets.

The least-squares refinement of the metal occupancies gives a precise structural formula of $(Fe_{0.94(1)}Co_{0.06(1)})$-$(Co_{0.95(1)}Fe_{0.05(1)})L^{Ph}$ for **4**, wherein a small degree of iron–cobalt mixing occurs at both metal-binding sites. As expected from the synthetic protocol, the cobalt is predominantly in the "bottom" binding pocket, featuring the tren donor set, while the iron is primarily located in the "top" binding pocket. Although mixing of iron and cobalt is observed at both metal-binding sites, the dominant metal accounts for 94 to 95% of the occupancy at each site. This degree of selectivity is somewhat remarkable considering the similarity of the ligand donors and the known lability of high-spin metal centers (vide infra). Of note, a recent study has exploited such lability to introduce cobalt center(s) into a preassembled triiron core as a synthetic route to iron–cobalt heterometallics.[70]

By taking the metal occupancies at the two binding sites and assuming purely statistical mixing, we can predict the percentages of each possible metal–metal pair. With this assumption, the single crystal of **4** comprises 89.3% $FeCoL^{Ph}$, 5.9% $CoCoL^{Ph}$, 4.5% $FeFeL^{Ph}$, and 0.3% $CoFeL^{Ph}$. Unfortunately, much higher data resolution would be needed in the crystal structure determination to fully model this four-component mixture. Hence, the bond distances and angles reported for **4** reflect this composite, of which the majority species is $FeCoL^{Ph}$. For simplicity, we discuss bond metrics of **4** with respect to its major component, but clearly, some uncertainty exist in these values because of their composite nature.

The solid-state structures of **3** and **4** are surprisingly similar. For instance, all the metal–ligand bond distances are within 0.019(3) Å, despite the swapping of cobalt with iron in the top binding pocket. The only significant change occurs in the M–

dx.doi.org/10.1021/ic400292g | Inorg. Chem. 2013, 52, 9216–9228

Table 2. Selected Distances (Å) and Angles (deg) for Experimental Bimetallic Structures: 1, 3, and 4

distances, angles	$Co_2(DPhF)_3$, **1**[19]	Co_2L^{Ph}, **3**	bonds, angles	$Fe_{0.99}Co_{1.01}L^{Ph}$, **4**[a]
Co–Co, Å	2.385(1)	2.2943(7)	Fe–Co, Å	2.1846(4)
Co–N_{eq}, Å	1.932(5)	1.923(2)	Co–N_{eq}, Å	1.927(1)
	1.955(5)			
	1.959(6)			
	1.957(5)	2.041(2)	Fe–N_{eq}, Å	2.0528(9)
	1.978(5)			
	1.983(5)			
Co–N_{ax}, Å		2.135(3)	Co–N_{ax}, Å	2.115(2)
Co-out of N_3-plane, Å	0.090	0.164	Co-out of N_3-plane	0.116
	0.065	0.186	Fe-out of N_3-plane	0.029
N_{eq}–Co–N_{eq}, deg	125.1(2)	119.28(2)	N_{eq}–Co–N_{eq}, deg	119.643(6)
	119.2(2)			
	115.6(2)			
	120.1(2)	119.18(2)	N_{eq}–Fe–N_{eq}, deg	119.982(1)
	114.8(2)			
	124.7(2)			
N_{eq}–Co–Co, deg	88.19(2)	84.77(5)	N_{eq}–Fe–Co, deg	89.20(3)
	88.24(2)			
	87.07(2)			
	90.06(2)	94.89(5)	N_{eq}–Co–Fe, deg	93.44(3)
	90.32(2)			
	91.30(2)			
N_{eq}–C–N_{eq}, deg	121.6(6)	116.8(2)	N_{eq}–C–N_{eq}, deg	116.9(1)
	122.7(6)			
	122.4(6)			

[a]Structure was determined from data collected using X-ray synchrotron radiation at 30 keV. See Experimental Section.

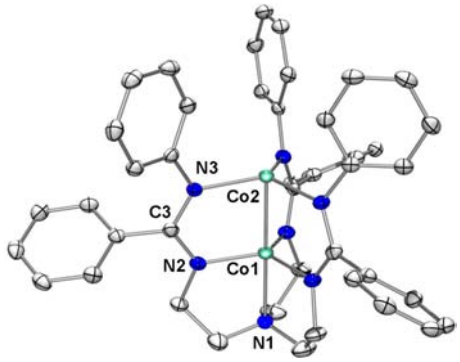

Figure 8. Solid-state structure of **3** at 50% probability. Hydrogen atoms are omitted for clarity. Selected bond distances (Å): Co1–Co2 2.2943(7), Co1–N2 1.923(2), Co1–N1 2.135(3), Co2–N3 2.041(2); selected bond angles (deg): N2–Co1–N2′ 119.28(2), N3–Co2–N3′ 119.18(2), N1–Co1–N2 85.11(5), N1–Co1–Co2 180.0, N2–Co1–Co2 94.89(5), N3–Co2–Co1 84.77(5); torsion (deg): N2–Co1–Co2–N3 4.57(7).

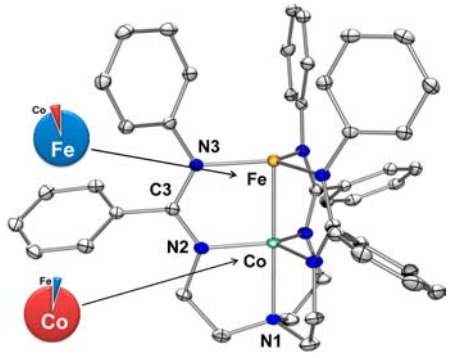

Figure 9. Solid-state structure of $Fe_{0.99}Co_{1.01}L^{Ph}$ **4** at 50% probability. Hydrogen atoms are omitted for clarity. The pie charts depict the percentages of iron and cobalt present at each metal binding site (as determined by X-ray anomalous dispersion). Selected bond distances (Å): Fe–Co 2.1846(4), Co–N2 1.927(1), Co–N1 2.115(2), Fe–N3 2.0528(9); selected bond angles (deg): N2–Co–N2′ 119.643(6), N3–Fe–N3′ 119.982(1), N1–Co–N2 86.56(3), N1–Co–Fe 180.0, N2–Co–Fe 93.44(3), N3–Fe–Co 89.20(3); torsion (deg): N2–Co–Fe–N3 4.30(3).

Co bond distance, which shortens from 2.2944(7) Å in **3** (M = Co) to 2.1846(4) Å in **4** (M = Fe). Correlated with the shorter M-M bond, the iron center is *less* displaced from the equatorial N_3-plane. If one considers that the covalent radius of iron is larger than that of cobalt, then the M-Co bond distance is expected to increase from **3** to **4**, which is opposite of what is observed. Hence, we ascribe the shorter Co–Fe bond to depopulating a d-electron from an M–Co antibonding orbital, which would increase the formal M-M bond order by 0.5. The iron–cobalt complex **4** is an unusual example of iron–cobalt bonding. Nearly all the structural examples of iron–cobalt bonds in the Crystallographic Structural Database are within carbonyl clusters, where the median Fe–Co bond distance is 2.55 Å.[71] Only a single molecule has Fe–Co bonds reasonably close to **4**: a trinuclear Fe_2Co core with a capping sulfide atom (Fe–Co 2.225 and 2.296 Å).[72]

Magnetic Measurements and EPR/Mössbauer Spectroscopy. Because spin states can be challenging to predict for metal–metal bonds of late first-row transition metals, we were interested in probing the effect of an apical donor and/or metal identity on the electronic structure of these metal–metal bonds. Owing to the high air-sensitivity of **1**, the assignment of its spin ground state had been based primarily on a theoretical

dx.doi.org/10.1021/ic400292g | Inorg. Chem. 2013, 52, 9216–9228

study.[25] SCF-Xα-SW calculations on the truncated molecule $Co_2(HNCHNH)_3$ favored the sextet spin.

We have investigated the variable temperature magnetic susceptibility measurements of the dicobalt complexes **1** and **3**, as shown in Figure 10. From ~50 to 290 K, the effective magnetic moment, μ_{eff}, is essentially temperature independent with values of 6.92 and 6.39 μ_B for **1** and **3**, respectively (χ^*T = 5.99 cm^3 K mol^{-1} for **1** and 5.11 cm^3 K mol^{-1} for **3**). These plots are consistent with an energetically well-isolated sextet state, which has a spin-only value of 5.92 μ_B. Hence, the data can be fitted using a single spin S = 5/2 Hamiltonian for the bimetallics **1** and **3**. The deviation of the μ_{eff} versus T plots from the spin-only value for **1** and **3** can be simulated by adopting electronic g values different from g = 2; best fits are obtained with $g_{5/2}$ = 2.33 and 2.16. Because the presence of any magnetic impurities can obscure true g-values in these static susceptibility measurements, more reliable g-values are obtained from EPR spectroscopy (vide infra).

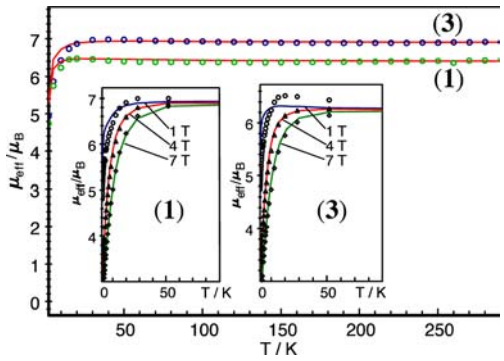

Figure 10. Temperature dependence of the effective magnetic moment, μ_{eff}, of **1** (green circles) and **3** (blue circles), at 1 T, from 2 to 290 K. The solid red lines represent the best fit. See text for simulation parameters. The insets show the result of multifield measurements recorded at 1, 4, and 7 T.

Below 50 K, the effective magnetic moments of **1** and **3** deviate from the high-temperature limit because of the combined effect of field saturation, zero-field splitting, and weak intermolecular interactions, which together can be reasonably simulated as shown in the inset of Figure 10. Indeed, weak intermolecular ferromagnetic coupling is best recognized as the small rise in $\mu_{eff}(T)$ around about 20 K. The effect was approximated by using a mean-field approximation with a Weiss-constant θ_w for parametrization. Best fits are obtained with zero-field splitting parameter $D_{5/2}$ = 9(±2) and 6(±3) cm^{-1} for the ground states of **1** and **3**, respectively. The corresponding values for θ_w are 1.5 K in both cases. We further note that the intermolecular interactions should be weak as the closest intermolecular M···M contacts are all greater than 8.5 Å (Supporting Information, Figure 10).

The EPR spectra of **1** and **3** have also been collected in frozen toluene at 20 K. Both complexes show similar axial derivative signals at effective g-values around g_{eff} = 6 and 2, which are typical of transitions within the m_s = ± 1/2 Kramers doublet of S = 5/2 systems with significant axial zero-field splitting ($D \gg h\nu$ at X-band, i.e., 0.3 cm^{-1}) and small-to-vanishing rhombicity, $E/D \approx 0$ (Figure 11). Under this condition, the ±3/2 and ±5/2 Kramers doublets are EPR-silent, and the shape of the spectra is independent of the actual value of the zero-field splitting parameter D. The spectra were simulated with the usual spin-Hamiltonian for the sextet spin state, and the axial zero-field splitting was fixed to correspond to the magnetic susceptibility measurements. (In the simulations, any value of $|D| > 2$ cm^{-1} was found to be consistent with the experimental spectra.) The electronic g values were constrained to be axial, ($g_1 = g_2$), such that the effects of weak rhombic splitting could be assigned to finite values of E/D (see Figure caption 11). The average of the g-values obtained from the EPR fits is 2.2 for both **1** and **3**, which is reasonably close in value to the average g-values used in the magnetic susceptibility fits.

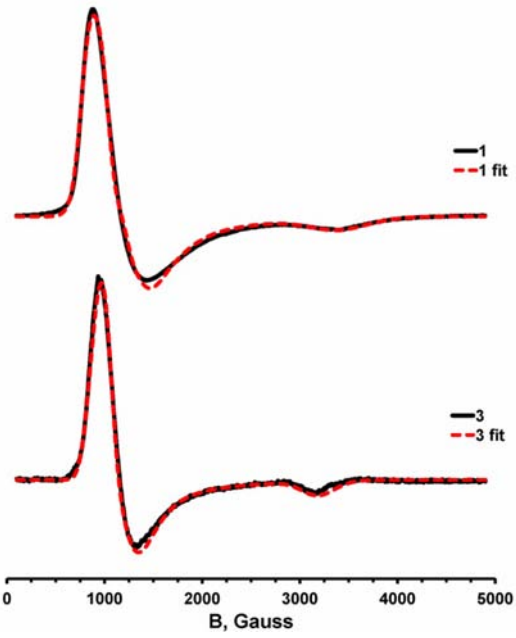

Figure 11. X-band EPR spectrum (dX''/dB) of **1** and **3** in toluene glass shown in blue (1.0 mM, 20.0 K, frequency = 9.646 GHz, modulation to 10 G, power = 2.01 mW). The spectrum was simulated (shown in red) by adopting S = 5/2 with the following anisotropic values: g = (2.243, 2.243, 2.12) for **1** and g = (2.201, 2.201, 2.215) for **3**; line widths, W = (172.6, 172.6, 700) for **1** and (184.2, 184.2, 400) for **3**. Zero-field splitting parameters: for **1**, D = 9 cm^{-1}, E/D = 0.0509; for **3**, D = 6 cm^{-1}, E/D = 0.0366 (D values fixed).

The sextet spin state is the highest spin configuration of a formally mixed-valent Co(II)Co(I) core. In the related high-spin diiron complex $Fe_2(DPhF)_3$, the Mössbauer spectra supported a fully delocalized Fe(1.5)Fe(1.5) configuration. By analogy, $Co_2(DPhF)_3$ should also have delocalized dicobalt core, Co(1.5)Co(1.5).

We anticipated that the iron−cobalt complex **4** would remain high spin because of the weak trigonal ligand field. The magnetic susceptibility data for **4** shows a temperature-independent magnetic moment of 6.73 μ_B (χ^*T = 5.68 cm^3 K mol^{-1}), which is consistent with S = 3 (Figure 12). The spin-Hamiltonian simulation yields a fitted g-value of 2.00, an axial zero-field splitting parameter, D_3 = 6 cm^{-1}, and θ_w = 3 K to model the weak intermolecular ferromagnetic coupling. Complex **4** coincidentally has a similar μ_{eff} value as **1** (perhaps because of the increased g value for the latter). But unlike **1**, **4** is expected to have integer spin, and indeed, it is EPR silent, which is consistent with the spin assignment.

As a cautionary note, the magnetic parameters reported for **4** have limited reliability because of the mixed metal composition. Also, we have found that the composition of the bulk material

dx.doi.org/10.1021/ic400292g | Inorg. Chem. 2013, 52, 9216−9228

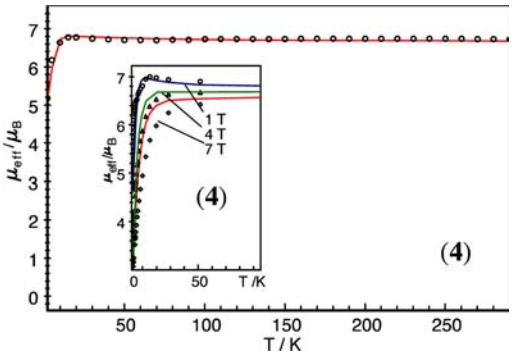

Figure 12. Temperature dependence of the effective magnetic moment, μ_{eff}, of **4** at 1 T, from 2 to 290 K. The solid lines represent the best fit for S_{tot} = 3 spin with g = 2 (χ_{TIP} = 1200 × 10^{-6} emu). For technical reasons (see Methods) the septet was simulated as the spin ground state of two ferromagnetically coupled spins $S_{1,2}$ = 3/2 with a large coupling constant, J = +200 cm^{-1}. The value renders the excited states at 1200 cm^{-1} such that thermal population of excited states is negligible, in accord with experiment. Formally the approach corresponds to the coupling of high-spin Fe(I) and Co(II), but such an interpretation is not meaningful since the septet state is energetically isolated and does not unveil its origin. The inset shows the result of a multifield measurement recorded at 1, 4, and 7 T.

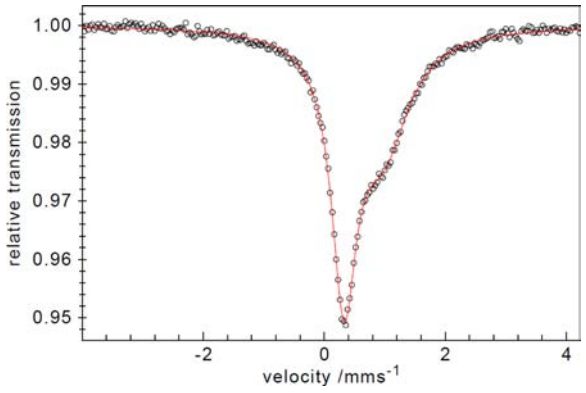

Figure 13. Zero-field Mössbauer spectrum of **4** at 80 K. The red solid line represents the best fit using two Lorentzian lines of equal intensity but different widths. Fitting parameters: δ = 0.65 mm/s, ΔE_Q = 0.64 mm/s, line width = 0.5 mm/s for the left line and 1.08 mm/s for the right one.

can vary significantly from $FeCoL^{Ph}$. For a separate batch of **4** that was analyzed by inductively coupled plasma optical emission spectrometry (ICP-OES), a composition consistent with $Fe_{0.79}Co_{1.11}L^{Ph}$ was determined. We suspect that the excess of cobalt relative to iron arises from the dicobalt **3** impurity, which was confirmed by ^{1}H NMR spectroscopy.

To our knowledge, this is a unique spin state for an Fe−Co bond; as mentioned above, virtually all known complexes with an Fe−Co distance less than 3.02 Å (the sum of covalent radii for high-spin Fe(II) and Co(II)) contain CO ligands, with most of the remainder bearing strong-field NO or Cp-type ligands, suggesting low-spin metal centers. A couple of exceptions are an Fe(III)Co(III)Fe(III) complex, with a long Fe−Co distance of 2.870(1) Å,[73] found to have an S = 1 ground state, and a salen-type Fe(II)−Co(II) complex with an S = 3/2 ground state, from weak antiferromagnetic coupling across an even longer M-M distance of 2.886(2) Å.[74] Another rare exception is a heterotrimetallic Fe_2Co complex, wherein the $[FeCo]^{5+}$ subunit, with a short Fe−Co distance of 2.29 Å, is proposed to have a triplet subspin. Thus, **4** is a rare example of a high-spin iron−cobalt bond.

Iron−cobalt **4** has also been characterized by Mössbauer spectroscopy as shown in Figure 13 (80 K, zero applied field). The spectrum is broad and asymmetric, but a similar phenomenon was previously observed with $Fe_2(DPhF)_3$. The asymmetry in the Mössbauer doublet can be attributed to paramagnetic relaxation effects and/or the presence of a diiron impurity. The isomer shift obtained from a provisional line fit, δ = 0.65 mm/s, is identical to that found for $Fe_2(DPhF)_3$, suggesting that the iron−cobalt complex is a fully delocalized Fe(1.5)Co(1.5) core. The quadrupole splitting, ΔE_Q = 0.64 mm/s, is slightly larger than that of $Fe_2(DPhF)_3$ (ΔE_Q = 0.32 mm/s), reflecting the slightly larger electric field gradient upon substituting iron with cobalt.

Theoretical Calculations. Previously, the electronic structure of the trigonal dicobalt compound was investigated using SCF-Xα-SW and ab initio methods on the truncated model, $Co_2(HNCHNH)_3$.[25] In a trigonal ligand field, the d-orbitals of two metal centers can combine maximally to form 1 σ, 2 π, and 2 δ metal−metal bonds. For $Co_2(HNCHNH)_3$, the electronic configuration of the sextet ground state, $(\sigma)^2(\pi)^4(\pi^*)^4(\sigma^*)^1(\delta)^2(\delta^*)^2$, indicated a Co−Co bond order of 0.5. The electronic structures of the dicobalt cores in **1** and **3** is expected to be similar since an apical donor should only slightly perturb the energies of the σ and σ * MOs.

On the other hand, the rarity of short Fe−Co bonds prompted us to further investigate **4** using computational methods, including DFT, CASSCF, and CASPT2 calculations. The geometry of the full molecule was optimized at the DFT level in several possible spin states, from S = 0 to S = 3. At all three levels of theory, the septet was confirmed as the ground spin state (Table 3). Also, the septet structure agrees quite well with the experimental structure (Supporting Information, Table 1). The only significant difference with respect to experiment is the slight distortion from C_3 symmetry.

Table 3. Calculated Relative Energies (kcal/mol) of 4 for All Possible Spin States at DFT, CASSCF, and CASPT2 Levels of Theory

	DFT	CASSCF	CASPT2
Singlet	15.94	8.53	18.07
Triplet	7.09	10.86	13.99
Quintet	5.58	11.80	11.42
Septet	0	0	0

Because the wave functions of metal−metal bonds tend to be multiconfigurational, CASSCF/CASPT2 calculations were used to determine the electronic configuration of **4**. The natural orbitals comprising the valence 3d-electrons are shown in the MO diagram in Figure 14. The MO diagram of **4**, however, lacks the δ and δ* MOs, which are replaced by localized d_{xy} and $d_{x^2-y^2}$ orbitals. The loss of the weak δ and δ* bonds is likely because of the energetic mismatch between iron and cobalt 3d-electrons. The ground-state wave function is dominated by one main configuration (84.9%): $(\sigma)^2(\pi)^4(\pi^*)^3(\sigma^*)^1$(Co d_{xy})^1(Co $d_{x^2-y^2}$)^1(Fe d_{xy})^1(Fe $d_{x^2-y^2}$)^1.

The main configuration predicts a formal Fe−Co bond order of 1, but a more accurate bond order can be calculated by taking into consideration the contributing minor configurations. For the total ground-state wave function, the natural orbital occupation numbers become: $(\sigma)^{1.88}(\pi)^{3.92}(\pi^*)^{2.98}(\sigma^*)^{1.01}$(Co

dx.doi.org/10.1021/ic400292g | Inorg. Chem. 2013, 52, 9216−9228

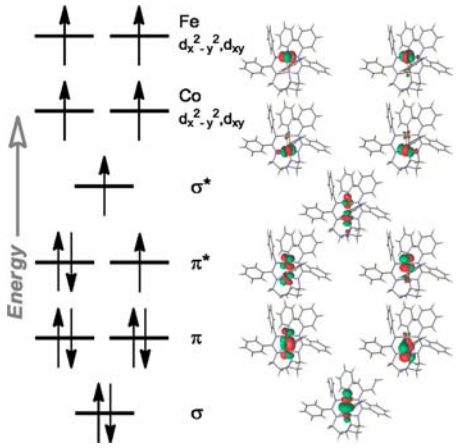

Figure 14. Qualitative MO diagram showing the natural orbitals for **4** that arise from CASSCF calculations. The dominating electronic configuration (84.9%) is shown.

$d_{xy})^{1.04}$(Co $d_{x^2-y^2})^{1.03}$(Fe $d_{xy})^{1.00}$(Fe $d_{x^2-y^2})^{1.00}$(Co 4d)$^{0.11}$(Co 4d)$^{0.03}$, which gives an effective bond order of 0.905 that is slightly lower than the formal bond order. Compared to dicobalt, the metal−metal bond order of iron−cobalt formally increases by half a π bond, which is consistent with the contraction of the M-M bond distance that is experimentally observed. On a related note, analysis of the orbital occupation numbers can give insight into the distribution of the 14 valence d-electrons between the iron and cobalt centers in **4**. The d-populations for iron and cobalt are 6.62 and 7.38, respectively (Supporting Information,Table 2). Thus, the CAS calculations support a highly delocalized Fe(1.5)Co(1.5) core.

4. CONCLUSIONS

Since their initial report, dicobalt (**1**) and diiron trigonal lanterns have been intriguing because of their short metal−metal bond distance, unusual high-spin electronic configurations, and mixed valency. Using a tris(amidinato)amine ligand, the dicobalt analogue (**3**) and a rare, mixed iron−cobalt complex (**4**) have been isolated. X-ray anomalous scattering techniques have proven useful to quantify the level of metal mixing in the heterobimetallic. While other bimetallics are present, including the dicobalt and diiron species, the iron−cobalt is the major component (89.3%). Collectively, the bimetallic tris(amidinate) systems illustrate that adding an apical amine donor or swapping one cobalt for iron (and vice versa) does not change the high-spin nature of the electronic ground state. Indeed, all the $[M_2]^{3+}$ cores herein are proposed to be fully delocalized, that is, M(1.5)M(1.5). One significant difference between dicobalt **3** to iron−cobalt **4** is the shortening of the metal−metal bond distance from 2.29 to 2.18 Å, respectively. The trend is consistent with a small gain in the metal−metal bond order (formally half) upon removing one antibonding d-electron from $[Co_2]^{3+}$ to obtain $[FeCo]^{3+}$. Finally, the two-step metalation strategy with the tris(amidinato)amine ligand is promising for gaining access to a larger family of homo- and heterobimetallic complexes.

■ ASSOCIATED CONTENT

Ⓢ Supporting Information

Crystallographic data in CIF format. Additional NMR spectroscopic characterization and computational data. This material is available free of charge via the Internet at http://pubs.acs.org.

■ AUTHOR INFORMATION

Corresponding Author

*E-mail: ebill@gwdg.de (E.B.), gagliard@umn.edu (L.G.), clu@umn.edu (C.C.L.).

Notes

The authors declare no competing financial interest.

■ ACKNOWLEDGMENTS

Andrew Fielding, Andreas Göbels, and Bernd Mienert are acknowledged for assisting with the acquisition of spectroscopic data. Professor Ted Betley is thanked for a helpful suggestion. C.M.Z. and C.C.L. thank Prof. John Lipscomb and Prof. David Blank for the use of their EPR and UV−vis-NIR instruments, respectively. X-ray diffraction experiments were performed using a crystal diffractometer acquired through an NSF-MRI award (CHE-1229400). Computing support and resources were provided by the Minnesota Supercomputing Institute, and funding for this work was provided in part by the University of Minnesota and the NSF (CHE-1254621). The computational results (H.J.K., D.Z., and L.G.) are based on work supported by the NSF (CHE-1212575). ChemMatCARS Sector 15 is principally supported by the NSF/DOE (CHE-0822838). Use of the Advanced Photon Source was supported by the U.S. Department of Energy, Office of Science, Office of Basic Energy Sciences, under Contract No. DE-AC02-06CH11357.

■ REFERENCES

(1) Farmer, J. A.; Campbell, C. T. *Science* **2010**, *329*, 933.
(2) Blackburn, N. J.; Barr, M. E.; Woodruff, W. H.; van der Ooost, J.; de Vries, S. *Biochemistry* **1994**, *33*, 10401.
(3) Lindahl, P. A. *J. Inorg. Biochem.* **2012**, *106*, 172.
(4) Nippe, M.; Goodman, S. M.; Fry, C. G.; Berry, J. F. *J. Am. Chem. Soc.* **2011**, *133*, 2856.
(5) Kadis, J.; Shin, Y.-g. K.; Dulebohn, J. I.; Ward, D. L.; Nocera, D. G. *Inorg. Chem.* **1996**, *35*, 811.
(6) Heyduk, A. F.; Macintosh, A. M.; Nocera, D. G. *J. Am. Chem. Soc.* **1999**, *121*, 5023.
(7) Dulebohn, J. I.; Ward, D. L.; Nocera, D. G. *J. Am. Chem. Soc.* **1990**, *112*, 2969.
(8) *Multiple Bonds Between Metal Atoms*, 3rd ed.; Cotton, F. A., Murillo, C. A., Walton, R. A., Eds.; Springer Science and Business Media, Inc.: New York, 2005.
(9) Nguyen, T.; Sutton, A. D.; Brynda, M.; Fettinger, J. C.; Long, G. J.; Power, P. P. *Science* **2005**, *310*, 844.
(10) Brynda, M.; Gagliardi, L.; Widmark, P.-O.; Power, P. P.; Roos, B. O. *Angew. Chem., Int. Ed.* **2006**, *45*, 3804.
(11) La Macchia, G.; Aquilante, F.; Veryazov, V.; Roos, B. O.; Gagliardi, L. *Inorg. Chem.* **2008**, *47*, 11455.
(12) La Macchia, G.; Li Manni, G.; Todorova, T. K.; Brynda, M.; Aquilante, F.; Roos, B. O.; Gagliardi, L. *Inorg. Chem.* **2010**, *49*, 5216.
(13) Kreisel, K. A.; Yap, G. P. A.; Dmitrenko, O.; Landis, C. R.; Theopold, K. H. *J. Am. Chem. Soc.* **2007**, *129*, 14162.
(14) Noor, A.; Wagner, F. R.; Kempe, R. *Angew. Chem., Int. Ed.* **2008**, *47*, 7246.
(15) Horvath, S.; Gorelsky, S. I.; Gambarotta, S.; Korobkov, I. *Angew. Chem., Int. Ed.* **2008**, *47*, 9937.
(16) Tsai, Y.-C.; Hsu, C.-W.; Yu, J.-S. K.; Lee, G.-H.; Wang, Y.; Kuo, T.-S. *Angew. Chem., Int. Ed.* **2008**, *47*, 7250.
(17) Hsu, C.-W.; Yu, J.-S. K.; Yen, C.-H.; Lee, G.-H.; Wang, Y.; Tsai, Y.-C. *Angew. Chem., Int. Ed.* **2008**, *47*, 9933.
(18) Jones, C.; Schulten, C.; Rose, R. P.; Stasch, A.; Aldridge, S.; Woodul, W. D.; Murray, K. S.; Moubaraki, B.; Brynda, M.; La Macchia, G.; Gagliardi, L. *Angew. Chem., Int. Ed.* **2009**, *48*, 7406.

(19) Cotton, F. A.; Daniels, L. M.; Maloney, D. J.; Matonic, J. H.; Murillo, C. A. *Inorg. Chim. Acta* **1997**, *256*, 283.
(20) Nguyen, T.; Merrill, W. A.; Ni, C.; Lei, H.; Fettinger, J. C.; Ellis, B. D.; Long, G. J.; Brynda, M.; Power, P. P. *Angew. Chem., Int. Ed.* **2008**, *47*, 9115.
(21) Fohlmeister, L.; Liu, S.; Schulten, C.; Moubaraki, B.; Stasch, A.; Cashion, J. D.; Murray, K. S.; Gagliardi, L.; Jones, C. *Angew. Chem., Int. Ed.* **2012**, *51*, 8294.
(22) Cotton, F. A.; Daniels, L. M.; Falvello, L. R.; Murillo, C. A. *Inorg. Chim. Acta* **1994**, *219*, 7.
(23) Cotton, F. A.; Daniels, L. M.; Maloney, D. J.; Murillo, C. A. *Inorg. Chim. Acta* **1996**, *249*, 9.
(24) Cotton, F. A.; Daniels, L. M.; Falvello, L. R.; Matonic, J. H.; Murillo, C. A. *Inorg. Chim. Acta* **1997**, *256*, 269.
(25) Cotton, F. A.; Feng, X.; Murillo, C. A. *Inorg. Chim. Acta* **1997**, *256*, 303.
(26) Brynda, M.; Gagliardi, L.; Roos, B. O. *Chem. Phys. Lett.* **2009**, *471*, 1.
(27) Roos, B. O.; Borin, A. C.; Gagliardi, L. *Angew. Chem., Int. Ed.* **2007**, *46*, 1469.
(28) Zall, C. M.; Zherebetskyy, D.; Dzubak, A. L.; Bill, E.; Gagliardi, L.; Lu, C. C. *Inorg. Chem.* **2012**, *51*, 728.
(29) Fout, A. R.; Basuli, F.; Fan, H.; Tomaszewski, J.; Huffman, J. C.; Baik, M.-H.; Mindiola, D. J. *Angew. Chem., Int. Ed.* **2006**, *45*, 3291.
(30) Cotton, F. A.; Daniels, L. M.; Feng, X.; Maloney, D. J.; Matonic, J. H.; Murilio, C. A. *Inorg. Chim. Acta* **1997**, *256*, 291.
(31) Lewis, R. A.; Morochnik, S.; Chapovetsky, A.; Wu, G.; Hayton, T. W. *Angew. Chem., Int. Ed.* **2012**, *51*, 12772.
(32) Mathialagan, R.; Kuppuswamy, S.; De Denko, A. T.; Bezpalko, M. W.; Foxman, B. M.; Thomas, C. M. *Inorg. Chem.* **2013**, *52*, 701.
(33) Fout, A. R.; Xiao, D. J.; Zhao, Q.; Harris, T. D.; King, E. R.; Eames, E. V.; Zheng, S.-L.; Betley, T. A. *Inorg. Chem.* **2012**, *51*, 10290.
(34) Clérac, R.; Cotton, F. A.; Dunbar, K. R.; Lu, T.; Murillo, C. A.; Wang, X. *Inorg. Chem.* **2000**, *39*, 3065.
(35) Clérac, R.; Cotton, F. A.; Dunbar, K. R.; Lu, T.; Murillo, C. A.; Wang, X. *J. Am. Chem. Soc.* **2000**, *122*, 2272.
(36) Berry, J. F.; Cotton, F. A.; Lu, T.; Murillo, C. A. *Inorg. Chem.* **2003**, *42*, 4425.
(37) Cooper, B. G.; Napoline, J. W.; Thomas, C. M. *Catal. Rev.* **2012**, *54*, 1.
(38) Kuppuswamy, S.; Cooper, B. G.; Bezpalko, M. W.; Foxman, B. M.; Powers, T. M.; Thomas, C. M. *Inorg. Chem.* **2012**, *51*, 1866.
(39) Bailey, P. J.; Coxall, R. A.; Dick, C. M.; Fabre, S.; Henderson, L. C.; Herber, C.; Liddle, S. T.; Loroño-González, D.; Parkin, A.; Parsons, S. *Chem.—Eur. J.* **2003**, *9*, 4820.
(40) Bergbreiter, D. E.; Killough, J. M. *J. Am. Chem. Soc.* **1978**, *100*, 2126.
(41) Spek, A. L. *Acta Crystallogr.* **2009**, *D65*, 148.
(42) Toby, B. H.; Von Dreele, R. B. *J. Appl. Crystallogr.* **2013**, *46*, 544.
(43) O'Connor, C. J. In *Progress in Inorganic Chemistry*; Lippard, S. J., Ed.; John Wiley & Sons, Inc.: New York, 1982; Vol. *29*, p 203.
(44) Weast, R. C.; Astle, M. J. *CRC Handbook of Chemistry and Physics*; CRC Press Inc.: Boca Raton, FL, 1979.
(45) Kahn, O. *Molecular Magnetism*; VCH Publishers, Inc.: Weinheim, Germany, 1993.
(46) Bill, E. *julX*; available from: http://ewww.mpi-muelheim.mpg.de/bac/logins/bill/julX_en.php.
(47) Roos, B. O.; Taylor, P. R.; Siegbahn, P. E. M. *Chem. Phys.* **1980**, *48*, 157.
(48) Andersson, K.; Malmqvist, P.-Å.; Roos, B. O. *J. Chem. Phys.* **1992**, *96*, 1218.
(49) Briggs, B. N.; McMillin, D. R.; Todorova, T. K.; Gagliardi, L.; Poineau, F.; Czerwinski, K. R.; Sattelberger, A. P. *Dalton Trans.* **2010**, *39*, 11322–11324.
(50) Ferrante, F.; Gagliardi, L.; Bursten, B. E.; Sattelberger, A. P. *Inorg. Chem.* **2005**, *44*, 8476.
(51) Gagliardi, L.; Roos, B. O. *Inorg. Chem.* **2003**, *42*, 1599.
(52) Poineau, F.; Forster, P. M.; Todorova, T. K.; Gagliardi, L.; Sattelberger, A. P.; Czerwinski, K. R. *Inorg. Chem.* **2010**, *49*, 6646.
(53) Perdew, J. P.; Zunger, A. *Phys. Rev. B* **1981**, *23*, 5048.
(54) A development of the University of Karlsruhe and Forschungszentrum Karlsruhe GmbH, 1989–2007, TURBOMOLE GmbH, since 2007: available from http://www.turbomole.com.
(55) Ahlrichs, R.; Bar, M.; Haser, M.; Horn, H.; Kolmel, C. *Chem. Phys. Lett.* **1989**, *162*, 165.
(56) Aquilante, F.; De Vico, L.; Ferré, N.; Ghigo, G.; Malmqvist, P.-Å.; Pedersen, T.; Pitonak, M.; Reiher, M.; Roos, B. O.; Serrano-Andrés, L.; Urban, M.; Veryazov, V.; Lindh, R. *J. Comput. Chem.* **2010**, *31*, 224.
(57) Roos, B. O.; Lindh, R.; Malmqvist, P.-Å.; Veryazov, V.; Widmark, P. O. *J. Phys. Chem. A* **2004**, *108*, 2851.
(58) Roos, B. O.; Lindh, R.; Malmqvist, P.-Å.; Veryazov, V.; Widmark, P. O. *J. Phys. Chem. A* **2005**, *109*, 6575.
(59) Hess, B. A. *Phys. Rev. A* **1986**, *33*, 3742.
(60) Aquilante, F.; Pedersen, T. B.; Lindh, R. *J. Chem. Phys.* **2007**, *126*, 11.
(61) Aquilante, F.; Pedersen, T. B.; Lindh, R.; Roos, B. O.; De Meras, A. S.; Koch, H. *J. Chem. Phys.* **2008**, *129*, 8.
(62) Aquilante, F.; Malmqvist, P.-Å.; Pedersen, T. B.; Ghosh, A.; Roos, B. O. *J. Chem. Theory Comput.* **2008**, *4*, 694.
(63) Forsberg, N.; Malmqvist, P.-Å. *Chem. Phys. Lett.* **1997**, *274*, 196.
(64) Lucas, R. L.; Zart, M. K.; Murkerjee, J.; Sorrell, T. N.; Powell, D. R.; Borovik, A. S. *J. Am. Chem. Soc.* **2006**, *128*, 15476.
(65) Ray, M.; Hammes, B. S.; Yap, G. P. A.; Rheingold, A. L.; Borovik, A. S. *Inorg. Chem.* **1998**, *37*, 1527.
(66) Jones, M. B.; MacBeth, C. E. *Inorg. Chem.* **2007**, *46*, 8117.
(67) Freedman, D. E.; Han, T. H.; Prodi, A.; Müller, P.; Huang, Q.-Z.; Chen, Y.-S.; Webb, S. M.; Lee, Y. S.; McQueen, T. M.; Nocera, D. G. *J. Am. Chem. Soc.* **2010**, *132*, 16185.
(68) Betley, T. A., personal communication.
(69) Wulf, R. *Acta Crystallogr., Sect. A: Found. Crystallogr.* **1990**, *46*, 681.
(70) Eames, E. V.; Hernández Sánchez, R.; Betley, T. A. *Inorg. Chem.* **2013**, *52*, 5006.
(71) Allen, F. *Acta Crystallogr., Sect. B* **2002**, *58*, 380.
(72) WanTao, Z.; Go-Shin; Syu-Tin, S. *Russ. J. Inorg. Chem.* **1997**, *42*, 1107.
(73) Glaser, T.; Beissel, T.; Bill, E.; Weyhermüller, T.; Schünemann, V.; Meyer-Klaucke, W.; Trautwein, A. X.; Wieghardt, K. *J. Am. Chem. Soc.* **1999**, *121*, 2193.
(74) Matsumoto, K.; Sekine, N.; Arimura, K.; Ohba, M.; Sakiyama, H.; Okawa, H. *Bull. Chem. Soc. Jpn.* **2004**, *77*, 1343.